MULTI-OBJECTIVE OPTIMIZATION OF LIQUID COLD PLATE WITH V-SHAPED RIBS FOR LITHIUM-ION BATTERYS

Yan WANG[a], Shaozhong LIANG[a], Jian FU[a], Jian ZHENG[a*], Ya WANG[b]

[a] School of Energy and Power Engineering, Lanzhou University of Technology, Lanzhou 730050, China

[b] Sinohydro Engineering Bureau 4 Co., Ltd, Power China, Xining 810009, China

*Corresponding author; Email: zhj16822@lut.edu.cn.

The performance of lithium-ion batteries is affected by the operational temperature significantly for the NEVs, and should be below 338 K and 5 K, respectively in the actual project. An efficient thermal management system is essential for the battery, as it would ensure the safe operation and increase the battery life. In this study, the LCP with V-shaped ribs is applied to improve the heat transfer characteristics for guaranteeing the safe operational temperature of the battery. Based on the battery thermal models, the accuracy of numerical simulation through classical experimental correlation is verified, and is adopted to investigate the effects of different design factors on the heat dissipation of the battery, including the ribbed shaped, the distance between adjacent ribs and the inlet velocity of the coolant. The maximum temperature and the temperature difference of the battery and the pressure drop of the channel are taken as the design objectives. An orthogonal test and an entropy weighted-TOPSIS method are used to optimize the results with multi-objective analysis, then the optimal case of design parameters is obtained. The optimal case for the LCP is the ribbed shape of Model 2, the distance between the adjacent ribs of 30 mm and the inlet velocity of 0.3 m/s. A good balance is achieved between the heat dissipation of the battery pack and the pressure drop of the channel. The optimal case can reduce the maximum temperature and the temperature difference of the battery by 7.41K and 4.94K compared with the unoptimized cases, meanwhile the pressure drop is also effectively controlled.

Key words*: Lithium-ion batteries, Liquid Cold plate, V-shaped ribs, Heat dissipation, Multi-objective optimization*

1. Introduction

The exhaust emitted from the Internal combustion engine (ICE) vehicles has become a problem that cannot be ignored with the growing severity of the global energy crisis and environmental pollution [1]. In this situation, the new energy vehicles (NEVs) are rapidly developing due to their advantages, such as environmental protection and energy saving, low noise, simple and compact structure [2]. It has received wide attention from governments around the world. The endurance and power performance, reliability and safety of the NEVs are directly affected by the battery as the core [3]. Operating temperature is the key factor affecting the performance of the battery [4]. The performance, life and capacity of the battery pack will be reduced by prolonged operation at high temperatures [5]. In addition, irreversible and destructive electrochemical reactions will occur inside

the battery [6], when a large amount of heat generated by the battery cannot be dissipated in time. It results in extensive short-circuiting and thermal runaway of the battery, and even cause the NEVs fires or explosions [7]. Therefore, an efficient battery thermal management system must be designed and optimized to ensure the battery operates safely and stably within an appropriate temperature range [8].

Liquid cooling is widely applied in the electronic equipment thermal management system due to the excellent heat transfer performance [9]. The main types of liquid cooling system are classified as direct contact and indirect contact. The direct contact is the method that directly immerses the battery in coolant, and the liquid cold plate (LCP) are used for heat dissipation of indirect contact types [10]. It is worth noting that the leakage and the corrosion are the drawback of direct contact type at long-term work, which will be a negative impact for the NEVs [11]. There are the advantages of the LCP, such as compact structure, low cost and safety. Therefore, the LCP is the main way to be applied in the liquid cooling system of the NEVs at present [26].

Optimizing the structural parameters of the LCP is the method that effectively improves the heat dissipation [13]. An experiment was carried out by Zhang [14], on a channel with the roughness elements. The central focus of their research was on investigating the influence of the rough elements on the flow and heat transfer characteristic. The result shows that the thermal performance is improved due to the eddy currents generated near the rough elements in the channel. In the early research [15], square cross-section straight ribs were mainly added on the surface of the channel to enhance the thermal performance. With the further study of heat transfer in channel with ribs, Kumar and Kim [16] investigated the flow and heat transfer characteristics by deploying the V-shaped ribs in the channel. The most important result of their study was that the boundary layer is effectively destroyed and the heat transfer was improved by the twist tape vortex generated of the V-shaped rib. In the space layout optimization, Promvonge [17]. investigated the convective heat transfer of the square-duct with the V-shaped ribs though a numerical simulation. The conclusions indicated that the secondary flow is enhanced by enhancing the flow pattern of the original flow region in the channel, and the convection heat transfer is further enhanced. Thus, the thermal performance of the discrete V-shaped ribs is higher than the continuous V-shaped ribs. Xu [18] experimentally studied the influence of different ribbed distance on the heat transfer characteristic and friction in the channel. They found that the thermal performance can be effectively increased by diminishing the distance between adjacent ribs, but at the same time the friction was increased. The orthogonal test was applied by Zhao [19], researched the influence of the LCP parameter structure on the heat dissipation of the battery pack. The outcome of their research was that the heat dissipation of the battery pack was significantly improved by increasing the width and height of the LCP channel. Wu [20] adopted the entropy weight-TOPSIS method for multi-objective analysis, the balance of the energy consumption and heat dissipation in the electronic equipment cooling system was obtained. The design parameter case of the optimizing heat dissipation and reducing energy consumption was obtained. In the previous studies, the channel with the V-shaped ribs was mostly employed in the large-scale heat exchangers to enhance the heat transfer [21]. There are few studies on the heat transfer of the small diameter LCP, and the research was limited to the analysis of a single factor and objective [22]. The multi-objective analysis coupling with the influence of multi-parameter was still insufficient in the actual engineering project of the battery liquid cooling system, which needs to the further research.

In this study, the effects of various design parameters for the LCP with V-shaped ribs on the heat dissipation of a battery pack. Key parameters include the rib shape, the spacing between adjacent ribs,

and the inlet fluid velocity. The design objectives focus on minimizing the maximum temperature and temperature differences across the battery pack while also reducing the energy consumption associated with pressure drops within the channels. An orthogonal test design is combined with the entropy weight-TOPSIS (Technique for Order Preference by Similarity to Ideal Solution) method to optimize these parameters. This research provides valuable insights and serves as a reference for the multi-objective optimization parameter design of LCP with V-shaped ribs for the battery.

2. Model and methodology

2.1 Model

In this study, the battery model is referenced from a practical engineering project [23]. The electrodes and other auxiliary devices are ignored, which can simplify the model to save the time in numerical simulation. The length d_1 of 148 mm, a width d_2 of 91mm, and a thickness d_3 of 27.5 mm in the battery. The battery pack model consists of twelve single batteries, and the LCP is deployed underneath the battery pack, as shown in Fig. 1. The detailed parameters of the battery are shown in Table 1.

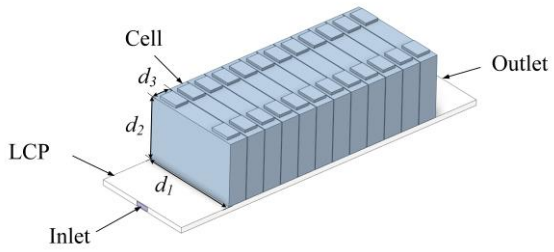

Fig. 1 Battery model

Table 1. Cell parameter

Parameters	Values
Nominal capacity [Ah]	40
Nominal voltage [V]	3.2
$d_1 \times d_2 \times d_3$ [mm]	148×91×27.5
Density [kgm^{-3}]	2160
Specific heat [$Jkg^{-1}K^{-1}$]	1129
Thermal conductivity [$Wm^{-1}K^{-1}$]	1/25/25

The LCP is shown in Fig. 2, it including four rectangular flow channels are added with V-shaped ribs. In the LCP, where d represents the width of the rectangular flow channel, α represents the angle between the ribs and the wall of the channel, and P represents the distance between the adjacent ribs, and the parameters of the LCP are shown [24]in Table 2

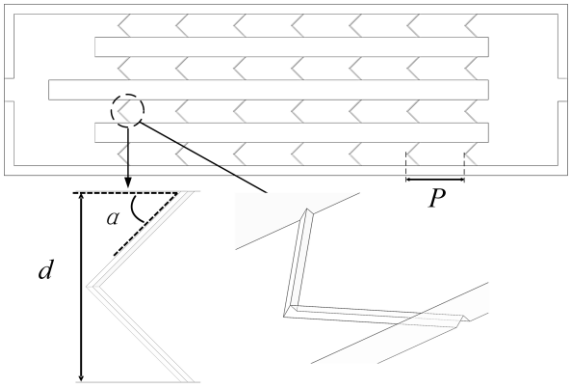

Fig. 2 Liquid cold plate

Table 2. Geometric parameters of LCP

Parameters	Values
LCP material	Aluminum
Plate length [mm]	470
Plate width [mm]	148
Channel width [mm]	20
Channel thickness [mm]	6
Rib angle [◦]	45
Rib thickness [mm]	1

2.2 Governing equations

2.2.1. Battery energy conservation

The heat will be generated by the battery pack during operation [25]. The energy conservation equation of the battery will be expressed as:

$$\rho_b c_b \frac{\partial T}{\partial t} = \frac{\partial}{\partial x}\left(\lambda_x \frac{\partial T}{\partial x}\right) + \frac{\partial}{\partial y}\left(\lambda_y \frac{\partial T}{\partial y}\right) + \frac{\partial}{\partial z}\left(\lambda_z \frac{\partial T}{\partial z}\right) + Q \quad (1)$$

where ρ_b is the density of battery, c_b is the specific heat capacity, and the material of battery is assumed to be anisotropic, λ_x, λ_y, λ_z are the thermal conduction coefficients [26] of length, width and thickness in the battery, respectively, T is the temperature, Q is the heat generation of the battery.

A large amount of heat is generated by the internal resistance and internal electrochemical reaction of the battery when operation for a long time. The equation of the battery heat generation is following [27]:

$$\dot{Q} = I\left[\left(U_{OCV} - U\right) + T\frac{\partial U_{OCV}}{\partial T}\right] \quad (2)$$

where I is the current, U_{OCV} and U is the open circuit voltage and operating voltage of the battery, respectively. The item $I(U_{OCV}\text{-}U)$ is the heat generated by the resistance and other irreversible reactions. The item $IT(\partial U_{OCV}/\partial T)$ is the heat generated by the electrochemical reaction inside the battery. In general, the heat generated by the electrochemical reaction of the battery is usually ignored in the studies, because it is far smaller than the heat generated by the resistance and other irreversible reactions [28]. Therefore, the heat exchange between the battery and the LCP during operation is expressed as:

$$Q = \frac{A}{\delta}(T_b - T_p) \tag{3}$$

where A is the contact area between the battery pack and the LCP, δ is the thermal conductivity, T_b and T_p represents the temperature of the battery and the LCP.

2.2.2 Liquid cold plate energy equation

The energy equation of the LCP is expressed as:

$$\rho_p c_{pp} \frac{\partial T_p}{\partial t} = \nabla \cdot \left(\lambda_p \nabla T_p \right) \tag{4}$$

where ρ_p is the density of water, c_{pp} is the thermal capacity, v is the inlet velocity, T_p is the temperature, λ_p is the thermal conductivity.

In this study, water is used as a coolant in the LCP of the battery pack. The continuity, momentum, and energy equations of the coolant can be expressed as: [29]

$$\nabla \cdot \vec{v} = 0 \tag{5}$$

$$\rho_c \left[\frac{\partial \vec{v}}{\partial t} + (\vec{v} \cdot \nabla)\vec{v} \right] = \rho_c f - \nabla p + \mu \nabla^2 \vec{v} \tag{6}$$

$$\rho_c c_{pc} \frac{\partial T_c}{\partial t} + \nabla \cdot \left(\rho_c c_{pc} v T_c \right) = \nabla \cdot \left(\lambda_c \nabla T_c \right) \tag{7}$$

The equation for the k-ε turbulence model can be expressed as [30]:

$$\rho_c \frac{\partial k}{\partial t} + \vec{\nabla} \cdot (\rho_c k \vec{v}) = \vec{\nabla} \cdot [(\mu + \frac{\mu}{\sigma_k}) \cdot \vec{\nabla}(k)] + 2\mu_t E_{ij}^2 - \rho_c \varepsilon \tag{8}$$

$$\rho_c \frac{\partial \varepsilon}{\partial t} + \vec{\nabla} \cdot (\rho_c \varepsilon \vec{v}) = \vec{\nabla} \cdot [(\mu + \frac{\mu}{\sigma_\varepsilon}) \cdot \vec{\nabla}(\varepsilon)] + 2C_1 \frac{\varepsilon}{k} \mu_t E_{ij}^2 - C_2 \rho_c \frac{\varepsilon^2}{k} \tag{9}$$

$$\mu_t = \rho_c C_\mu \frac{k^2}{\varepsilon} \tag{10}$$

where C_1, C_2, C_3, σ_k and σ_ε are the constants of the model, k represents the turbulent kinetic energy, ε represents the turbulent dissipation rate, μ_t represents the turbulent viscosity, and E_{ij} represents the deformation rate and ∇ represent the gradient operator.

The equation of channel pressure drop is expressed as [30]:

$$\Delta p = \frac{\rho_c L_p f_p v^2}{D} \tag{11}$$

where f_p is the friction factor, D is the hydraulic diameter of the channel, L_p is the length of the channel.

2.3 Parameter definition

Nu is a dimensionless parameter that reflects the heat transfer characteristics of the LCP. An increasing *Nu* indicates that the convection heat transfer is becoming more effective. Its equation is expressed as follows:

$$Nu = \frac{hD}{\lambda_c} \tag{12}$$

$$h = \frac{q_c}{A_{\text{wall}} \left(T_w - T_m \right)} \tag{13}$$

where q_w is the wall heat flux, A_{wall} is the area of the heat exchange wall of channel, T_w is the temperature of wall, T_m is the average temperature of the fluid.

$$TI = \frac{v'}{v_m} \tag{14}$$

where v' is the velocity fluctuation and v_m is the mean velocity along the mainstream in the channel.

2.4 Boundary conditions and grid independence validation

2.4.1 Boundary conditions

The commercial software FLUENT 2021R1 and the workstation with 52 cores are used for numerical simulation in this study. The calculation of heat transfer is employed only for the domain composed of the battery pack, LCP and water to simplify. It is assumed that the LCP material is homogenous and isotropic, and the fluid is incompressible. The inlet velocity boundary condition and the outflow boundary condition are considered. The initial temperature of inlet is set to 300 K, the inlet gauge pressure is set to 0 Pa, and the inlet velocity is set according to the specific example given. The inner wall of channel is no slip, and the adiabatic boundary condition is considered for the contact surface with air.

Different ribbed shapes are shown in Fig. 3, including the continuous V-shaped ribs (Model 1), the V-shaped ribs broken and staggered (Model 2), the V-shaped rib truncated on both sides (Model 3), the V-shaped ribs broken in the middle (Model 4) and the smooth channel (Model 0). Moreover, *P* are set to 20 mm、30 mm、40 mm、50 mm and 60 mm, the inlet *v* are set to 0.1 m/s、0.2 m/s、0.3 m/s、0.4 m/s、0.5 m/s.

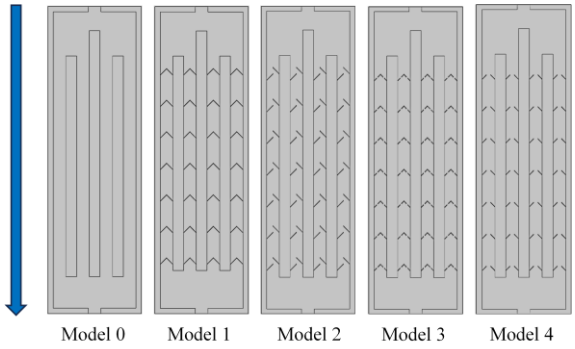

Fig. 3 Different ribbed shapes in the LCP

2.4.2 Grid independence validation

As shown in Fig. 4, the polyhedral grid is applied in the whole mesh model. The grid boundary layer between the solid domain and the fluid domain is refined to obtain more accurate calculation. In addition, the independence of the grids must be verified to ensure the accuracy of the numerical simulation. The maximum temperature and the temperature difference of the battery pack in different grids number are shown in Fig. 5. The maximum temperature and the temperature difference of the battery pack dropped sharply as the number of grids increased from 2×10^5 to 1.13×10^6. It can be observed that the highest difference corresponding to these grids is only 0.02 K as the number of grids increases from 1.13×10^6 to 4.56×10^6. It has been proven that increasing the number of grids enhances the precision of numerical simulation. However, increasing the number of grids excessively will not significantly improve the accuracy, but will greatly increase the time of the numerical simulation. Therefore, the model of grids number 1.13×10^6 is used for the numerical simulation in this study.

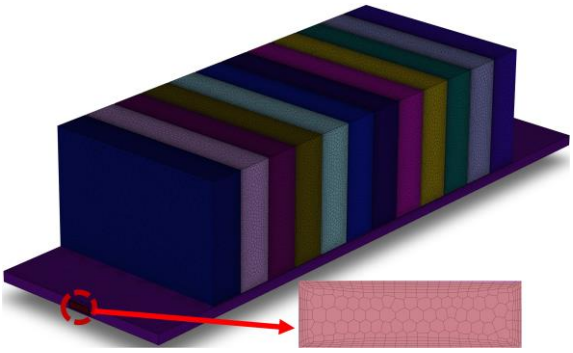

Fig. 4 The mesh model of the battery pack.

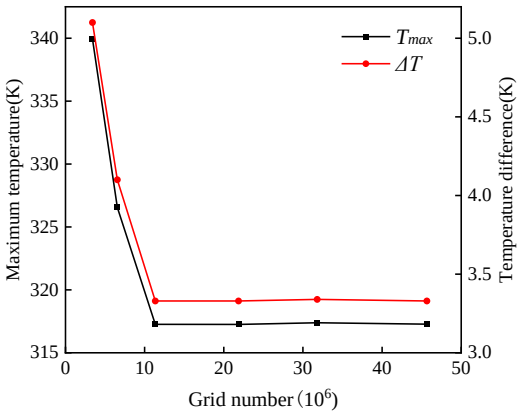

Fig. 5 Grid independence validation results

3. Results and discussion

The heat dissipation and the maintenance of temperature uniformity are the two main roles of the LCP for the battery pack. The potential safety hazard for the NEVs will be posed when the operating temperature of the battery pack exceeds safe levels. In actual engineering projects, the maximum temperature and the temperature difference of the battery pack should be below 338 K and 5 K, respectively[31] to ensure safe and stable operation of the battery. In addition, the flow of coolant is driven by the pump to remove the heat of the battery in the LCP. The consumption of the battery pack will be increased with the workload of the pump rise, due to the flow resistance in the channel. Therefore, considering the overall efficiency of the NEVs, the pressure drop of the channel should be reduced, meanwhile ensuring that the maximum temperature and the temperature difference of the battery are effectively reduced.

3.1 Model verification

The accuracy of numerical simulation is verified though classical experimental correction. The Sieder-Tate correlation [32] is generally adopted to calculate the local *Nu* for the convective heat transfer of laminar flow in a smooth channel. The equation can be express as:

$$Nu_0 = 1.86\left(\frac{\mathrm{Re}_0 \mathrm{Pr}_0}{L/D}\right)^{1/3}\left(\frac{\mu_c}{\mu_w}\right)^{0.14} \tag{15}$$

The qualitative temperature is the average fluid temperature T_m in the correlation, T_w is calculated according to the wall temperature, L represents the length of the flow channel, and D represents the characteristic length. *Re* is Reynolds number, *Pr* is the Prandtl number. The agreement between the

numerical results and the correlation results are shown in Fig. 6, and the error between the numerical and correlation results is maintained at about 2%.

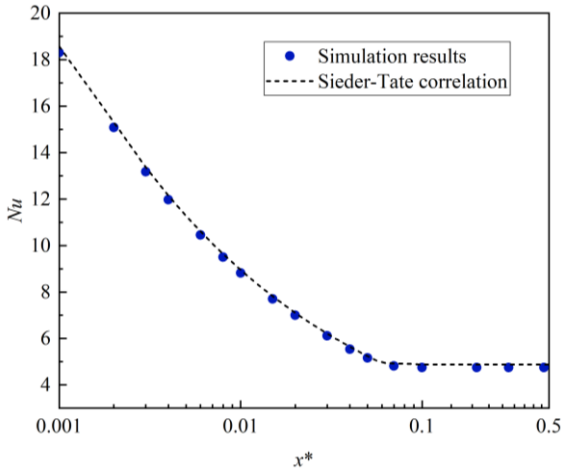

Fig. 6 The result of the simulation and Sieder-Tate correlation

3.2 The effect of the coolant inlet velocity

In this section, five different inlet velocities are set to investigate the heat dissipation effect of the LCP for the battery pack. *Re* = 1846, the flow is laminar [24], and *Re* = 2769, the *k*-*ε* turbulence model is considered. The temperature distributions of the battery with different inlet velocity of the coolant are shown in Fig. 7. The results of the maximum temperature, the temperature difference and the pressure drop with the inlet velocity of the coolant are shown in Fig. 8. It indicates that the maximum temperature and the temperature difference of the battery pack are decreased with the inlet velocity rising. The downward trend in the maximum temperature and the temperature difference is very obvious when the inlet velocity of coolant varies between v = 0.1 m/s to v = 0.3 m/s. It is decreased from 321.14 K and 6.11 K to 313.88 K and 1.28 K, respectively. This is due to the convective heat transfer coefficient increases as the inlet velocity increases. Notably, the heat dissipation effect of the LCP on the battery pack has reached the actual operating temperature required at v = 0.3 m/s. However, there is a slight downward trend when the inlet velocity increases further. It is only respectively reduced by 0.6 K and 0.46 K compared with the v = 0.3 m/s. At the same time, there is the obvious rising in the pressure drop can be observed as the inlet velocity increases, the energy consumption of the battery pack is also increased. The outcome is that the heat dissipation of the LCP can be effectively improved by increasing the inlet velocity of the coolant. However, the temperature of the battery pack not be reduced infinitely as the increasing of the inlet velocity. It also increases the pressure drop, further increasing the energy consumption of the battery pack. Excessive inlet velocity of the coolant should not be used when considering the efficiency of the battery pack.

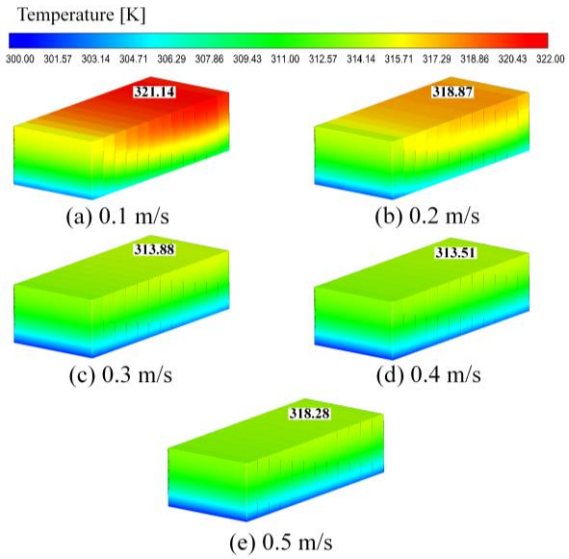

Fig. 7 The temperature contours of the battery pack with different inlet velocity

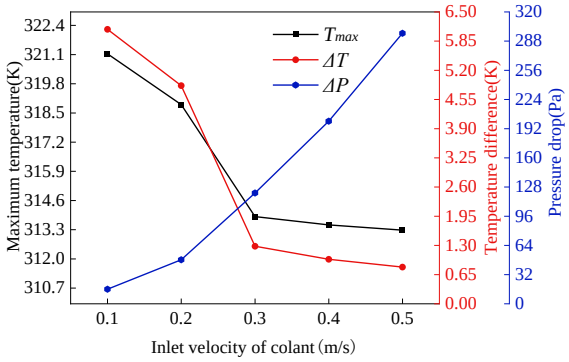

Fig. 8 The maximum temperature, the temperature difference and the pressure drop with different inlet velocity

3.3 The effect of the ribbed shape

The fluid will be interfered and the streamline will be changed by the V-shaped ribs in the channel, and forming the multi-longitudinal swirl [33] and enhancing the intensity of the second flow. In addition, the fluid flow from the wall boundary region to the core region to enhance the mixing of fluid. It results in the enhanced heat transfer of the LCP [33]. Therefore, the difference in the ribbed shape will further lead to different heat transfer characteristics of the LCP, and affecting the heat dissipation on the battery pack.

The temperature distributions of the battery pack with different ribbed shapes are shown in Fig. 9. The results of the maximum temperature, the temperature difference and the pressure drop with different V-shaped ribs are shown in Fig. 10. It can be observed that the maximum temperature and the temperature difference of the battery pack on the LCP with Model 2 are lower than others. The heat transfer of the LCP with Mode 0 is the weakest. The maximum temperature and the temperature difference of the battery pack with Model 1, which are reduced by 1.18 K and 1.03 K compared with Model 0. The maximum temperature and the temperature difference of the battery pack with Model 3, which are 1.07 K and 0.93 K lower than that of Model 0. The maximum temperature and the temperature difference of the battery pack with Model 4 are 320.53 K and 5.58 K, respectively, which are 0.61 K and 0.53 K lower than that of Model 0. In summary, the LCP with Model 2 has the greatest

heat transfer characteristic on the battery pack, which can effectively achieve the heat dissipation requirements.

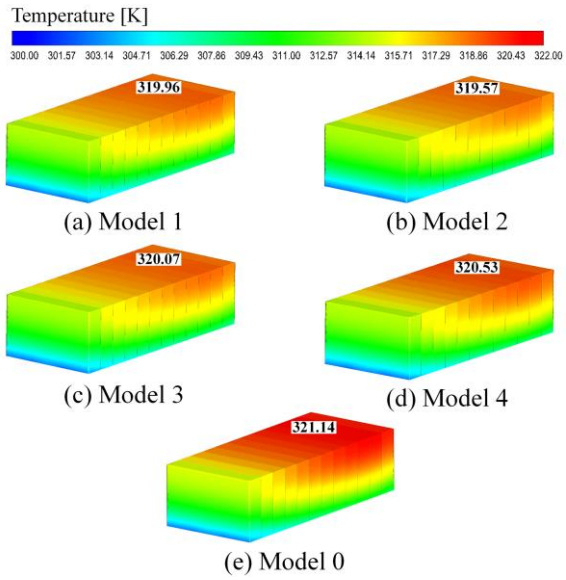

Fig. 9 The temperature distributions of the battery pack of different ribbed shapes

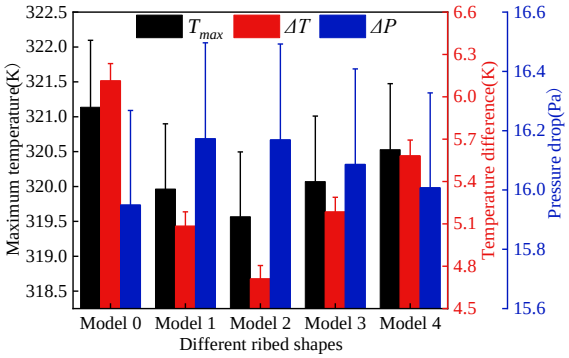

Fig. 10 The maximum temperature, the temperature difference and the pressure drop with different ribbed shapes. (Confidence level 2%)

The local *Nu* distributions of different ribbed shapes in the same spatial position of the channel are shown in Fig. 11 (a). The local *TI* distributions of the different ribbed shapes are shown in Fig. 11 (b). It can be observed that the local *Nu* of Model 0 is uniformly distributed entirely, and there is no obvious high heat transfer region, because there is no effective interference with the fluid in smooth channel. A high heat transfer region occurs behind the rib when the fluid flows through the rib of Model 1. Since the secondary flow in these regions are enhanced by the twisted tape vortex [24] generated of the near-rib. There is a low heat transfer region in the boundary region due to the presence of the boundary layer, the secondary flow is weak or does not generate. The vortex in the region behind the rib is weakened due to the effect of shorter rib on the flow structure becoming weaker [35]. It results in that the secondary flow is weakened behind the rib region. Meanwhile, the secondary flow along the rib from the core region to the boundary region is weakened in advance. Therefore, the local *Nu* of Model 3 and Model 4 along the downstream lower than Mode l remarkably. Notably, the disturbance effect of Model 2 is stronger than other ribs due to staggered in the channel.

The region of vortex is increased at the downstream of the rib, which effectively enhances the secondary flow, and the heat transfer characteristics is enhanced with the turbulence intensity increases. The heat transfer is more uniform as the high heat transfer region can cover the large areas behind the rib in the channel with Model 2.

The turbulent intensity is effectively enhanced by the ribbed shaped change, which improves the heat transfer. The maximum temperature of the battery pack is effectively reduced by the LCP with Model 2, and maintain the temperature uniformity. Meanwhile, the pressure drop of the channel is increase as the effect of the rib on the flow structure improves. A further comprehensive analysis is needed to balance the heat dissipation and the energy consumption of the battery pack.

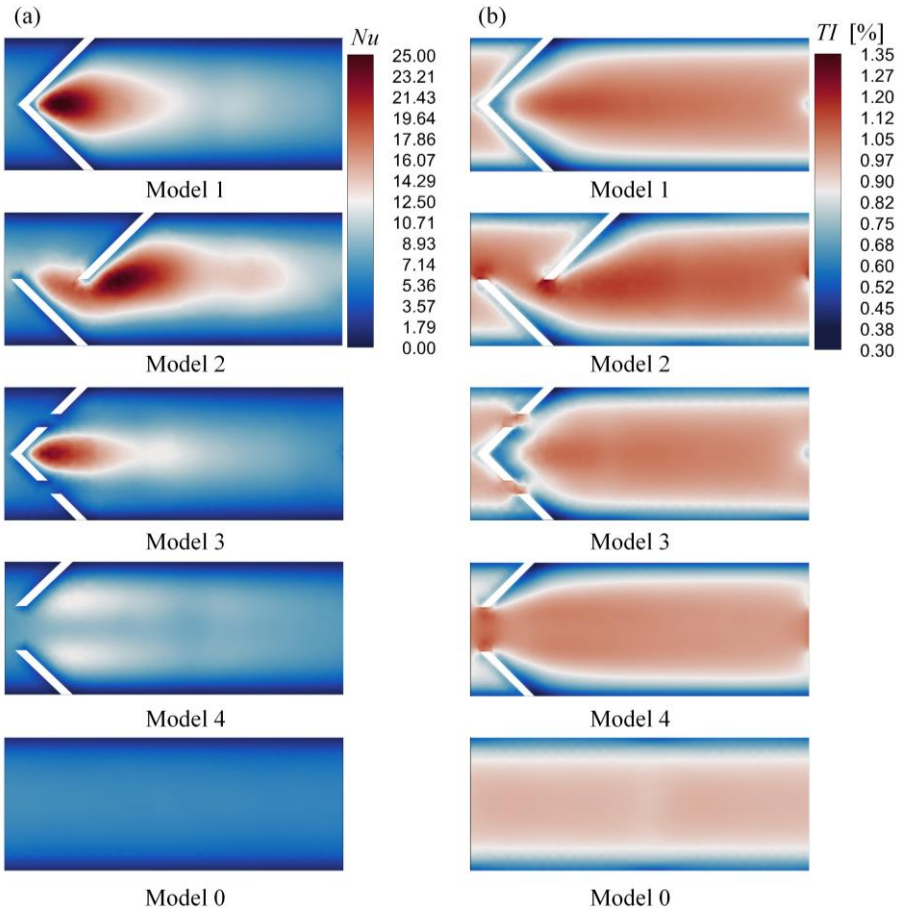

Fig. 11 (a) Local *Nu* distributions of different ribbed shapes, (b) Local *TI* of different ribbed shapes

3.4 The effect of distance between adjacent ribs

The distance between adjacent ribs reflects the density of the rib arranged along the mainstream direction. The heat transfer characteristic and the pressure drop of the LCP are affected by the density of ribs. The LCP with Model 2 is employed to analyze the effect of the distance between adjacent ribs. The temperature distributions of the battery pack with the distance between adjacent ribs are shown in Fig. 12. The results of the maximum temperature, the temperature difference and the pressure drop with the distance between adjacent ribs are shown in Fig. 13. It can be observed that the maximum temperature and the temperature difference of the battery pack are decreased with the ribbed distance decrease. The maximum temperature and the temperature difference are respectively reduced from 319.92 K and 5.02 K to 318.37 K and 3.82 K, as the distance between adjacent ribs from 60 mm to 20

mm. It can be attributed to shortening the distance between adjacent ribs, which enhances the disturbance of fluid between ribs and prevents the development of the boundary layer. The high heat transfer region in the channel is increased, thus the heat transfer characteristic of the LCP is enhanced. In addition, the pressure drop also increases from 16.06 Pa to 17.42 Pa. Therefore, the structural design of the LCP should consider the overall efficiency. The energy consumption can be reduced by increasing the ribbed distance while ensuring the effective heat dissipation of the battery pack.

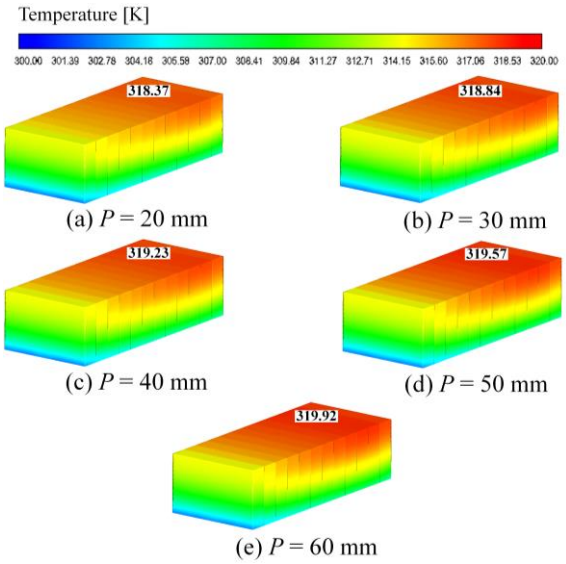

Fig. 12 The temperature distributions of the battery pack with different distance of ribs

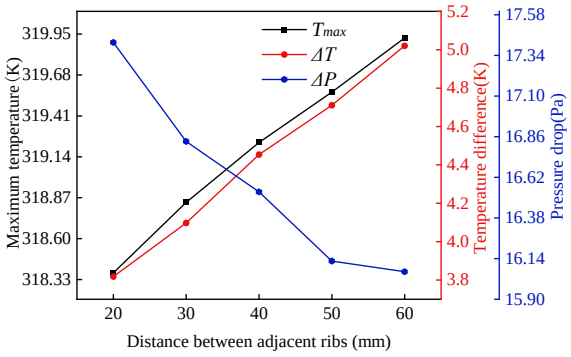

Fig. 13 The results of the maximum temperature, the temperature difference and the pressure drop of the battery pack with different distance of ribs

4. Multi-objective optimization

The single factor analysis in Section 3 showed that the ribbed shapes, the ribbed distance and the inlet velocity affect the heat transfer characteristic of the LCP. It is not possible to improve the heat transfer of the LCP by changing a single design parameter in the actual project. The orthogonal test is employed to estimate the importance of the design parameters to the heat transfer of the LCP. In addition, the entropy weight-TOPSIS method is used to calculate the weights of each design targets from the orthogonal test results, and the multi-objective analysis is further carried out to obtain the optimal case.

4.1 Orthogonal test analysis

The orthogonal test schedule is shown in Table 3, and the ribbed shape, the ribbed distance and the inlet velocity are represented as factors A, B, C. The results are shown in Table 4. The range analysis results of T_{max}, ΔT and ΔP are shown in Table 5, Table 6 and Table 7, respectively. The greater the R_i is the greater the impact of the factor on the design targets. The equation can be expressed as [36]:

$$K_{ij} = \sum_{j=1} T_{maxij} (i = A, B, C;\ j = 1, 2, 3, 4) \tag{16}$$

$$k_{ij} = \frac{1}{n} K_{ij} (i = A, B, C;\ j = 1, 2, 3, 4) \tag{17}$$

$$R_j = max(K_{ij}) - min(k_{ij}) (i = A, B, C;\ j = 1, 2, 3, 4) \tag{18}$$

where i represents the design factor, j represents the level of design factors, n represents the number of levels, R_j represents the degree of influence of design factors on the result.

The standard deviation S_c is used to reflect the discrete degree of level on the design targets to quantify the importance of the factor [37]. Its equation can be expressed as follows:

$$S_c = \sqrt{\frac{\sum_{j=1}^{n} (k_{ij} - \frac{1}{n} \sum_{n=1}^{n} k_{ij})}{n}} \tag{19}$$

The results show that the R_i and S_c of design factor C are the largest, and the R_i and S_c of design factor B are the smallest for the maximum temperature and the temperature difference of the battery pack.

Therefore, the order of design factors affecting the maximum temperature and the temperature difference of the battery pack are ranked as C > A > B. The influence of the inlet velocity is the greatest on the maximum temperature and the temperature difference of the battery pack, while the influence of the ribbed distance is the smallest. Therefore, the optimal combination of factors is $A_3B_5C_1$. From this point of view, the parameter combination of Model 2, P = 20 mm, v = 0.5 m/s. The influence of design factors on the pressure drop also is ranked as C > A > B, the optimal combination of factors is $A_1B_1C_1$, the parameter combination of Model 0 and v = 0.1 m/s.

The battery is still in the equilibrium state of continuous heat dissipation to the liquid cold plate at the end of the numerical simulation. Therefore, the amount of heat transferred by the battery to the LCP in unit time have been calculated. The heat dissipation values for all the profiles as shown in Table 8. The temperature of the battery lower indicates the heat dissipation effect of the LCP is better. The heat transferred from the battery to the LCP becomes smaller when the temperature difference between the battery and the liquid cold plate becomes small. However, the pressure drop of the LCP will be increased when the heat dissipation effect of the battery pack is better. The pressure drop of the LCP should be reduced, meanwhile ensuring that the maximum temperature and the temperature difference of the battery are effectively reduced to considering the overall efficiency of the NEVs is the focus of this study. The results should be further optimized with multi-objective analysis to obtained the optimal case of design parameters.

Table 3. Orthogonal test schedule

Level	Factors		
	A	B	C
1	0	20	0.1

2	1	30	0.2
3	2	40	0.3
4	3	50	0.4
5	4	60	0.5

Table 4. Orthogonal test results

Number	Factors			Results		
	A	B	C	T_{max}(K)	ΔT(K)	ΔP(Pa)
1	0	20	0.1	321.14	6.11	15.95
2	0	30	0.3	319.72	5.34	121.38
3	0	40	0.5	318.87	4.86	296.60
4	0	50	0.2	317.6	4.12	48.17
5	0	60	0.4	313.88	1.28	200.14
6	1	20	0.5	313.04	0.67	322.01
7	1	30	0.2	316.34	2.57	51.56
8	1	40	0.4	313.38	0.92	203.89
9	1	50	0.1	319.97	5.08	16.17
10	1	60	0.3	313.84	1.27	123.75
11	2	20	0.4	313.24	0.82	221.30
12	2	30	0.1	318.84	4.1	16.83
13	2	40	0.3	313.73	1.17	125.75
14	2	50	0.5	313.15	0.74	303.69
15	2	60	0.2	316.85	3.69	50.07
16	3	20	0.3	313.69	1.16	128.97
17	3	30	0.5	313.14	0.74	311.88
18	3	40	0.2	316.97	2.03	51.10
19	3	50	0.4	313.45	0.96	197.99
20	3	60	0.1	320.29	5.37	16.13
21	4	20	0.2	316.14	2.35	52.40
22	4	30	0.4	313.4	0.92	203.81
23	4	40	0.1	320.31	5.37	16.21
24	4	50	0.3	313.86	1.28	122.14
25	4	60	0.5	313.24	0.81	301.88

Table 5. K_{in}, R_i, and S_c of the T_{max}.

	Factors		
	A	B	C
K_{i1}	1591.21	1577.25	1600.55
K_{i2}	1576.57	1581.44	1574.84
K_{i3}	1575.81	1583.26	1571.44
K_{i4}	1577.54	1578.03	1583.90
K_{i5}	1576.95	1578.10	1567.35

k_{i1}	318.24	315.45	320.11
k_{i2}	315.31	316.29	314.97
k_{i3}	315.16	316.65	314.29
k_{i4}	315.51	315.61	316.78
k_{i5}	315.39	315.62	313.47
R_i	3.08	1.20	6.64
S_c	1.16	0.46	2.36

Table 6. K_{in}, R_i, and S_c of the ΔT.

	Factors		
	A	B	C
K_{i1}	21.71	11.11	26.03
K_{i2}	10.51	13.67	10.22
K_{i3}	10.52	14.35	7.82
K_{i4}	10.26	12.18	14.76
K_{i5}	10.73	12.42	4.90
k_{i1}	4.34	2.22	5.21
k_{i2}	2.10	2.73	2.04
k_{i3}	2.10	2.87	1.56
k_{i4}	2.05	2.44	2.95
k_{i5}	2.15	2.48	0.98
R_i	2.29	0.65	4.23
S_c	0.90	0.23	1.48

Table 7. K_{in}, R_i, and S_c of the ΔT

	Factors		
	A	B	C
K_{i1}	1004.26	740.64	81.30
K_{i2}	717.39	705.46	622.00
K_{i3}	717.64	693.56	1536.06
K_{i4}	706.08	688.16	253.31
K_{i5}	696.45	691.98	1027.13
k_{i1}	200.85	148.13	16.26
k_{i2}	143.48	141.09	124.40
k_{i3}	143.53	138.71	307.21
k_{i4}	141.22	137.63	50.66
k_{i5}	139.29	138.40	205.43
R_i	61.56	10.50	290.95
S_c	23.64	3.85	105.62

Table 8. The heat dissipation values

Number	Factors			Heat dissipated values
	A	B	C	

1	0	20	0.1	201.39 J/s
2	0	30	0.3	187.624 J/s
3	0	40	0.5	187.6 J/s
4	0	50	0.2	202.211 J/s
5	0	60	0.4	187.61 J/s
6	1	20	0.5	186.26 J/s
7	1	30	0.2	191.2 J/s
8	1	40	0.4	187.453 J/s
9	1	50	0.1	197.87 J/s
10	1	60	0.3	198.005 J/s
11	2	20	0.4	186.526 J/s
12	2	30	0.1	193.77 J/s
13	2	40	0.3	186.32 J/s
14	2	50	0.5	186.87 J/s
15	2	60	0.2	191.42 J/s
16	3	20	0.3	187.13 J/s
17	3	30	0.5	186.99 J/s
18	3	40	0.2	190.23 J/s
19	3	50	0.4	187.2 J/s
20	3	60	0.1	200.15 J/s
21	4	20	0.2	188.85 J/s
22	4	30	0.4	187.53 J/s
23	4	40	0.1	198.91 J/s
24	4	50	0.3	187.58 J/s
25	4	60	0.5	187.7 J/s

4.2 Entropy weight-TOPSIS analysis

The entropy weight technique for order preference by similarity to ideal solution (TOPSIS method) is that approximates the optimal solution by extracting the entropy in the data. It can objectively determine the weight among multiple targets and carry out the comprehensive analysis [38].

First, the evaluation matrix of TOPSIS is constructed, and the decision matrix of the evaluation scheme is set as follows:

$$X = \begin{matrix} x_{11} & x_{12} & \cdots & x_{1n} \\ x_{11} & x_{22} & \cdots & x_{2n} \\ \vdots & \vdots & \vdots & \vdots \\ x_{m1} & x_{m2} & \cdots & x_{mn} \end{matrix} \tag{20}$$

The data in the decision matrix is normalized to ensure that all features are equivalent, so that its value is in [0,1].

The obtained decision matrix is regularized, and the matrix $R=(r_{ij})_{m\times n}$ is obtained. The equation can be expressed as follows:

$$r_{ij} = \frac{x_{ij}}{\sqrt{\sum_{i=1}^{m} x_{ij}^2}} \tag{21}$$

The entropy weight method is used to determine the weight of the target, and the information entropy of each index is calculated. The equation can be expressed as:

$$\mathrm{e}_j = -\frac{1}{\ln(m)} \sum_{i=1}^{m} p_{ij} \ln(p_{ij}) \tag{22}$$

The difference coefficient of the target can be obtained from the entropy value e*j*, which can be expressed as:

$$d_j = 1 - \mathrm{e}_j \tag{23}$$

The weight equation of each design object is determined by the difference coefficient:

$$w_j = \frac{d_j}{\sum_{k=1}^{n} d_k} \tag{24}$$

Relative approximation η_i [39] indicates the degree of approximation between the evaluation scheme and the positive and negative ideal solutions. The larger η_i is, the closer the scheme is to the ideal solution. Combined with the weights of each evaluation scheme determined above, regularization weighting is carried out, and the result is $v_{ij}=w_{ij}r_{ij}$. The equation for calculating the positive and the negative ideal solutions are expressed as follows:

$$S_j^+ = \min_{1 \le i \le m} \{v_{ij}\} n = 1, 2, \ldots, n \tag{25}$$

$$S_j^- = \min_{1 \le i \le m} \{v_{ij}\} n = 1, 2, \ldots, n \tag{26}$$

The Euclidean distance between each evaluation scheme and the positive and negative ideal solution is adopted, and its equation is:

$$Sd_i^+ = \sqrt{\sum_{j=1}^{n} (S_j^+ - r_{ij})^2} i = 1, 2, \ldots, m \tag{27}$$

$$Sd_i^- = \sqrt{\sum_{j=1}^{n} (S_j^- - r_{ij})^2} i = 1, 2, \ldots, m \tag{28}$$

The equation for calculating the degree of proximity can be expressed as follows:

$$\eta_i = \frac{Sd_i^-}{Sd_i^+ + Sd_i^-} i = 1, 2, \ldots, m \tag{29}$$

It can be observed from the orthogonal test that the influence sequence of factors on T_{max}, ΔT and ΔP is same, all of which are ranked as C > A> B. However, for T_{max} and ΔT, the best factor combination scheme is $A_3B_1C_5$. For ΔP, the optimal factor combination scheme is $A_1B_1C_1$. The entropy weight-TOPSIS method is applied to analyze the results, to optimize the design parameters.

The weights of T_{max}, ΔT and ΔP are 34.31%, 46.47% and 19.22% respectively. The degree of proximity of the optimal ideal scheme at 25 groups of schemes is further obtained, as shown in Table 9. The optimal case for the LCP is the ribbed shape of Model 2, the ribbed distance of 30 mm, and the inlet velocity of 0.3 m/s. A good balance is achieved between the heat dissipation and the energy consumption in this case.

Table 9. TOPSIS results

Number	Sd_i^+	Sd_i^-	η_i	Rank
1	0.578	0.192	0.250	23
2	0.494	0.154	0.238	24
3	0.470	0.144	0.235	25
4	0.354	0.284	0.445	18
5	0.133	0.518	0.796	9
6	0.192	0.576	0.750	13
7	0.217	0.401	0.649	16
8	0.121	0.555	0.821	6
9	0.478	0.217	0.312	20
10	0.093	0.529	0.851	3
11	0.130	0.564	0.812	8
12	0.383	0.275	0.418	19
13	0.087	0.538	0.860	1
14	0.181	0.578	0.762	10
15	0.306	0.323	0.514	17
16	0.088	0.539	0.860	2
17	0.186	0.568	0.753	12
18	0.205	0.425	0.674	15
19	0.119	0.551	0.823	5
20	0.506	0.205	0.289	21
21	0.197	0.419	0.680	14
22	0.121	0.554	0.820	7
23	0.506	0.205	0.288	22
24	0.093	0.528	0.851	4
25	0.180	0.561	0.757	11

5. Conclusion

The LCP with V-shaped ribs is designed in the present study to optimize the heat dissipation effect of the battery pack. The effects of design parameters of the LCP on the heat dissipation of the battery pack are analyzed though a numerical simulation, such as the ribbed shape and the ribbed distance of the LCP and the inlet velocity of the coolant. The optimal parameter combination is obtained by the multi-objective analysis. The conclusions are as follows:

(1) The maximum temperature and the temperature difference of the battery pack can be effectively reduced by increasing the inlet velocity of the coolant and reducing the distance between adjacent ribs. However, the downward trend will slow down, and the flow channel pressure drop will increase when the inlet velocity exceeds 0.3 m/s and the ribbed distance increase to 30 mm.

(2) The effect of heat dissipation of the LCP with Model 2 (The V-shaped rib broken and staggered) is the greatest. The maximum temperature and the temperature difference of the battery pack are reduced by 1.57 K and 1.4 K, respectively, compared with the smooth channel of the LCP.

(3) The entropy weight-TOPSIS method is applied to conduct a multi-objective comprehensive analysis of the results, and the optimal case of design parameters is obtained. The optimal case of

parameters for the LCP is the ribbed shape of Model 2, the distance between adjacent ribs of 30 mm and the inlet velocity of 0.3 m/s. A good balance is achieved between the heat dissipation and the energy consumption of the battery pack. The optimal case can reduce the maximum temperature and the temperature difference of the battery by 7.41K and 4.94K compared with the unoptimized cases, and the pressure drop of the channel is effectively controlled.

Acknowledgments

This research was supported by the National Natural Science Foundation of China (Grant No. 52276197), Gansu Province Key Research and Development Program – Industrial Project (Grant No. 23YFGA0069) and Gansu Youth Science and Technology Fund (23JRRA827).

Nomenclature

T	Temperature (K)	E_{ij}	deformation rate
I	Current (A)	q	Heat flux (W/m^2)
U	Voltage (V)	∇	Gradient operator
Q	Heat generation of the battery (W)	TI	Turbulent intensity
d	Battery size (mm)	R	Range
P	Distance between adjacent ribs (mm)	Sd_i^+	Distance of positive ideal solution
v	Inlet velocity (m/s)	Sd_i^-	Distance of negative ideal solution
p	Pressure (Pa)	η_i	Degree of proximity
ρ	Density (kg/m^3)	μ	Dynamic viscosity [kg/(m·s)]
c_p	specific heat capacity (J/ (kg· K))	*Greek letters*	
f	Friction factor	α	Rib angle (°)
L	Length (mm)	λ	Thermal conductivity [W/(m·K)]
D	Hydraulic diameter (mm)	*Subscripts*	
ΔP	Channel pressure drop (Pa)	b	Battery
Nu	Nusselt number	p	Plate
TI	Turbulence intensity	c	Coolant
Re	Reynolds number	*Abbreviations*	
Pr	Prandtl number	NEV	New energy vehicles
h	Heat transfer coefficient (W/m^2·K)	ICE	Internal combustion engine
A	Area (m^2)	LCP	Liquid cold plate
k	Turbulent kinetic energy	TOPSIS	Technique for order preference by similarity to ideal Solution
ε	Turbulent dissipation rate		

References

[1] Darcovich, K., *et al*. Comparison of cooling plate configurations for automotive battery pack thermal management, *Applied Thermal Engineering* 155 (2019), pp. 185-195.

[2] Fu Y, Min H., *et al*. Integrated testing of electric vehicle thermal management and optimization of flow field uniformity in air supply system. *Thermal Science*, pp. 2024 (00): 45-45.

[3] Rao, Z. H., *et al*. Experimental investigation on thermal management of electric vehicle battery with heat pipe, *Energy Conversion and Management* 65 (2013), pp. 92-97.

[4] Liu, B. H., *et al*. Safety issues and mechanisms of lithium-ion battery cell upon mechanical abusive loading: A review, *Energy Storage Materials* 24 (2020), pp. 85-112.

[5] Narayanasamy M P., *et al*. Heat transfer analysis of looped micro heat pipes with graphene oxide nanofluid for Li-ion battery, *Thermal Science*, (2021), pp. 25(1 Part A): 395-405.

[6] Fang H, Xu J., *et al*. Comparative analysis of cooling effect of battery module cooling plate structures. *Thermal Science*, pp. (2023) (00): 166-166.

[7] Liu, H. Q., *et al*. Thermal issues about Li-ion batteries and recent progress in battery thermal management systems: A review, *Energy conversion and management* 150 (2017), pp 304-330.

[8] Li F. Simulation of temperature field and optimization of heat dissipation structure for lithium-ion power battery pack based on multi-objective function optimization. *Thermal Science*, pp. (2024), 28(2 Part B): 1263-1270.

[9] Miao J., *et al*. Experimental and numerical analysis of variable cross-section channel liquid cooling plate for server chips thermal management. *Thermal Science and Engineering Progress*, pp. (2024), 49: 102470.

[10] Pesaran, A. A., Battery thermal management in EV and HEVs: issues and solutions, *Battery Man* 43.5 (2001), pp 34-49.

[11] Li, Y. T., *et al*. Optimization of thermal management system for Li-ion batteries using phase change material, *Applied Thermal Engineering* 131 (2018), pp 766-778.

[12] Zuo W., *et al*. Performance comparison between single S-channel and double S-channel cold plate for thermal management of a prismatic LiFePO4 battery. *Renewable Energy (*2022), pp.192: 46-57.

[13] Zhao, D., *et al*. Research on battery thermal management system based on liquid cooling plate with honeycomb-like flow channel, *Applied Thermal Engineering* 218 (2023), pp. 119324.

[14] Zhang C., *et al*. Effects of roughness elements on laminar flow and heat transfer in microchannels, *Chemical Engineering and Processing: Process Intensification* (2010), pp.49(11): 1188-1192.

[15] Lu, B., *et al*. Experimental and numerical investigation of convection heat transfer in a rectangular channel with angled ribs, *Experimental Thermal and Fluid Science* 30.6 (2006), pp. 513-521.

[16] Kumar, A., *et al*. Thermohydraulic performance of rectangular ducts with different multiple V-rib roughness shapes: A comprehensive review and comparative study, *Renewable and Sustainable Energy Reviews* 54 (2016), pp. 635-652.

[17] Promvonge, P., *et al*. Numerical heat transfer study of turbulent square-duct flow through inline V-shaped discrete ribs, *International Communications in Heat and Mass Transfer* 38.10 (2011), pp. 1392-1399.

[18] Xu, G. Q., *et al*. Effect of rib spacing on heat transfer and friction in a rotating two-pass square channel with asymmetrical 90-deg rib turbulators, *Applied Thermal Engineering* 80 (2015), pp. 386-395.

[19] Zhao, D., *et al*. Structure optimization of liquid-cooled plate for electric vehicle lithium-ion power batteries, *International Journal of Thermal Sciences* 195 (2024), pp. 108614.

[20] Wu, C. T., *et al*. Innovative liquid cooling channel enhanced battery thermal management (BTM) structure based on stepwise optimization method, *Journal of Energy Storage* 81 (2024), pp. 110485.

[21] Khoshvaght-Aliabadi M., *et al*. CFD study of rib-enhanced printed circuit heat exchangers for precoolers in solar power plants' supercritical CO2 cycle. Energy, pp. (2024), 292: 130418.

[22] Song H., et al. Numerical simulation of thermal performance of cold plates for high heat flux electronics cooling. *Thermal Science*, pp. (2023) (00): 261-261.

[23] Ding, Y. Z., *et al*. "Effect of liquid cooling system structure on lithium-ion battery pack temperature fields, *International Journal of Heat and Mass Transfer* 183 (2022), pp. 122178.

[24] Jiang, W., *et al*. Heat transfer performance enhancement of liquid cold plate based on mini V-shaped rib for battery thermal management, *Applied Thermal Engineering* 189 (2021), pp. 116729.

[25] Vali M P S N., *et al*. Comparison study on cooling management of composite phase change material battery pack: Two different cases. *Thermal Scienc*e, pp. 2023 (00): 218-218.

[26] Ding, Y. H., *et al*. Effect of liquid cooling system structure on lithium-ion battery pack temperature fields, *International Journal of Heat and Mass Transfer* 183 (2022), pp. 122178.

[27] Khan, S. A., *et al*. Design of a new optimized U-shaped lightweight liquid-cooled battery thermal management system for electric vehicles: A machine learning approach, *International Communications in Heat and Mass Transfer* 136 (2022), pp. 106209.

[28] Li, B., *et al*. Analysis of heat dissipation performance of battery liquid cooling plate based on bionic structure, *Sustainability* 14.9 (2022), pp. 5541.

[29] Deng, T., *et al*. Thermal performance of lithium-ion battery pack by using cold plate, *Applied Thermal Engineering* 160 (2019), pp. 114088.

[30] Xu, X. M., *et al*. Numerical study and optimizing on cold plate splitter for lithium battery thermal management system, *Applied Thermal Engineering* 167 (2020), pp. 114787.

[31] Fan, Y. W., *et al*. Numerical investigation on lithium-ion battery thermal management utilizing a novel tree-like channel liquid cooling plate exchanger, *International journal of heat and mass transfer* 183 (2022), pp. 122143.

[32] Clark S H, Kays W M. Laminar-flow forced convection in rectangular tubes, *Transactions of the American Society of Mechanical Engineers*, pp. (1953), 75(5): 859-866.

[33] Xiao, H., *et al*. Turbulent heat transfer enhancement in the mini-channel by enhancing the original flow pattern with v-ribs, *International Journal of Heat and Mass Transfer* 163 (2020), pp. 120378.

[34] Tanda, G. Heat transfer in rectangular channels with transverse and V-shaped broken ribs, *International Journal of Heat and Mass Transfer* 47.2 (2004), pp. 229-243.

[35] Xiao H., *et al*. A study on the mechanism of convective heat transfer enhancement based on heat convection velocity analysis. *Energies*, (2019), pp. 12(21): 4175.

[36] Pan, C. F., *et al.* Structure optimization of battery module with a parallel multi-channel liquid cooling plate based on orthogonal test, *Journal of Electrochemical Energy Conversion and Storage* 17.2 (2020), pp. 021104.

[37] Jia qiang E., *et al.* Orthogonal experimental design of liquid-cooling structure on the cooling effect of a liquid-cooled battery thermal management system. *Applied Thermal Engineering*, (2018), pp.132: 508-520.

[38] Satı, Z. E. Comparison of the criteria affecting the digital innovation performance of the European Union (EU) member and candidate countries with the entropy weight-TOPSIS method and investigation of its importance for SMEs, *Technological Forecasting and Social Change* 200 (2024), pp. 123.

[39] Chen H, An Y. Green Residential Building Design Scheme Optimization Based on the Orthogonal Experiment EWM-TOPSIS,. *Buildings*, pp. 2024, 14(2): 452.

Paper submitted: 23.07.2024
Paper revised: 01.09.2024
Paper accepted: 06.09.2024